

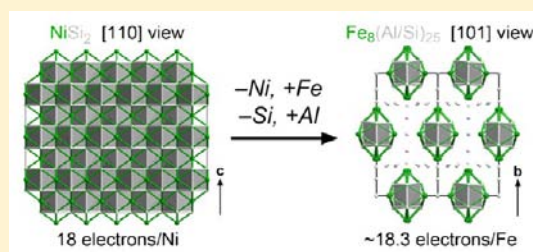
Fragmentation of the Fluorite Type in $\text{Fe}_8\text{Al}_{17.4}\text{Si}_{7.6}$: Structural Complexity in Intermetallics Dictated by the 18 Electron Rule

Rie T. Fredrickson and Daniel C. Fredrickson*

Department of Chemistry, University of Wisconsin—Madison, 1101 University Avenue, Madison, Wisconsin 53706, United States

Supporting Information

ABSTRACT: This Article presents the synthesis, structure determination, and bonding analysis of $\text{Fe}_8\text{Al}_{17.4}\text{Si}_{7.6}$. $\text{Fe}_8\text{Al}_{17.4}\text{Si}_{7.6}$ crystallizes in a new monoclinic structure type based on columns of the fluorite (CaF_2) structure type. As such, the compound can be seen as part of a structural series in which the fluorite structure—adopted by several transition metal disilicides (TMSi_2)—is fragmented by the incorporation of Al. Electronic structure analysis using density functional theory (DFT) and DFT-calibrated Hückel calculations indicates that the fluorite-type TMSi_2 phases (TM = Co, Ni) exhibit density of states (DOS) pseudogaps near their Fermi energies. An analogous pseudogap occurs for $\text{Fe}_8\text{Al}_{17.4}\text{Si}_{7.6}$, revealing that its complex structure serves to preserve this stabilizing feature of the electronic structure. Pursuing the origins of these pseudogaps leads to a simple picture: the DOS minimum in the TMSi_2 structures arises via a bonding scheme analogous to those of 18 electron transition metal complexes. Replacement of Si with Al leads to the necessity of increasing the (Si/Al):TM ratio to maintain this valence electron concentration. The excess Si/Al atoms are accommodated through the fragmentation of the fluorite type. The resulting picture highlights how the elucidating power of bonding concepts from transition metal complexes can extend into the intermetallic realm.



INTRODUCTION

Electron counting rules, and the bonding schemes with which we rationalize them, are fundamental to the chemist's search for order in the staggering range of compounds encountered in nature or chemical synthesis. This holds true not only for molecular chemistry, but also in the field of alloys and intermetallic phases. Since the pioneering work of Hume-Rothery, electron count has been identified as a key factor in determining the structure and properties of metallic compounds.¹ For the majority of these phases, however, the bonding schemes underlying their preferred electron counts remain obscure. The success of the Zintl concept in rationalizing the structures resulting from polar combinations of metals demonstrates the potential of the octet and Wade-Mingos rules for elucidating the role of electron count.² How might other molecular approaches to electron counting apply to intermetallic compounds?

In this Article, we describe the crystal structure and bonding of the new intermetallic phase $\text{Fe}_8\text{Al}_{17.4}\text{Si}_{7.6}$, whose complex structure can be simply understood using the 18 electron rule of transition metal (TM) complexes. Despite its ubiquity in organometallic and coordination compounds and its general origins in the nine valence orbitals of TM atoms,³ few examples have been noted of the 18 electron rule being obeyed by intermetallic compounds. Such a picture has been recognized as leading to a band gap and semiconducting properties in half-Heusler phases at 18 electrons/TM atom, but for these phases electron counts as high as 22/TM have been observed without structural consequences.⁴ With the structure of $\text{Fe}_8\text{Al}_{17.4}\text{Si}_{7.6}$ we

see to our knowledge the first example of intermetallic structural chemistry arising from a desire to maintain an 18 electron count.

Our original interest in TM–Al–Si phases began with a casual examination of the structure of $\text{Fe}_{25}\text{Al}_{78}\text{Si}_{20}$ (Figure 1).⁵ In looking at the connectivity between the main-group atoms in this structure, we noticed a intriguing pattern: the $\text{Fe}_{25}\text{Al}_{78}\text{Si}_{20}$ structure is based on a primitive cubic lattice similar to the Si-sublattices of the fluorite-type structures of CoSi_2 ⁶ and NiSi_2 .^{6b,7} However, this pattern is interrupted by inclusions of the fcc structure, a theme noted earlier by Häussermann et al. in the V_8Ga_{41} structure type.⁸

With these structural observations in hand, it is tempting to view $\text{Fe}_{25}\text{Al}_{78}\text{Si}_{20}$ as one of a number of possible geometrical perturbations of TMSi_2 fluorite structures. This idea prompted us to carry out synthesis in TM–Al–Si systems in search of other members of such a series.

The TM–Al–Si systems (TM = Fe, Co) have been the focus of intense study. In addition to $\text{Fe}_{25}\text{Al}_{78}\text{Si}_{20}$, distinct crystal structures have been reported for compounds with compositions near $\text{Fe}_{45}\text{Al}_{168}\text{Al}_{24}$,⁹ $\text{Fe}_2\text{Al}_9\text{Si}_2$,¹⁰ FeAl_3Si_2 ,¹¹ $\text{FeAl}_{2.7}\text{Si}_{2.3}$,¹¹ FeAl_2Si ,¹² $\text{Fe}_{1.7}\text{Al}_4\text{Si}$,¹³ $\text{Fe}_2\text{Al}_3\text{Si}_3$,¹⁴ $\text{Fe}_3\text{Al}_2\text{Si}_3$,¹⁵ $\text{Fe}_3\text{Al}_2\text{Si}_4$,^{15a} $\text{Fe}_2\text{Al}_3\text{Si}$,^{15b} $\text{Co}_3\text{Al}_3\text{Si}_4$,¹⁶ $\text{Co}_4\text{Al}_8\text{Si}$,¹⁷ Co_2AlSi_2 ,¹⁶ $\text{Co}_{19}\text{Al}_{43}\text{Si}_{12}$,¹⁸ and $\text{Co}_5(\text{Al/Si})_{16}$.^{18b,19} As could be guessed from this impressive list of structures, the phase diagrams for these ternary systems are complicated, and many of their details

Received: July 11, 2012

Published: September 17, 2012

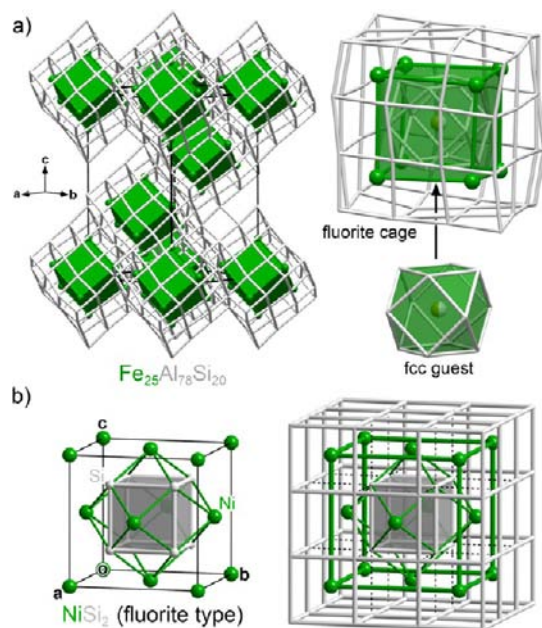


Figure 1. The crystal structure of $\text{Fe}_{25}\text{Al}_{78}\text{Si}_{20}$, which inspired our investigation of TM–Al–Si systems. (a) The structure can be viewed as a fluorite host framework with inclusions of the fcc structure. (b) Comparison with fluorite-type NiSi_2 structure shows that the fcc guests take the place of $\text{TM}_6(\text{Si}/\text{Al})_8$ units in $\text{Fe}_{25}\text{Al}_{78}\text{Si}_{20}$.

remain to be resolved.²⁰ Reported phases with unknown structures include $\text{Fe}_{2.2}\text{Al}_4\text{Si}_{3.8}$, $\text{Fe}_2\text{Al}_2\text{Si}_1$, $\text{Fe}_4\text{Al}_4\text{Si}_3$, $\text{Co}_3\text{Al}_4\text{Si}_2$, and $\text{Co}_3\text{Al}_5\text{Si}_2$.

In our pursuit of these unknown structures we carried out syntheses in the Fe–Si–Al and Co–Si–Al systems and determined two new crystal structures: those of $\text{Fe}_8\text{Al}_{17.4}\text{Si}_{7.6}$ and $\text{Co}_4\text{Al}_{5.5}\text{Si}_{2.8}$. Both compounds adopt new structural variants of the TMSi₂ fluorite type, in which the fluorite structure is cut into narrow infinite columns. $\text{Fe}_8\text{Al}_{17.4}\text{Si}_{7.6}$, the main subject of this Article, does not appear to belong to any of the listed compounds of the Fe–Al–Si system. It is instead closely related to FeAl_2Si , adopting a different superstructure of the same basic cell. On the basis of its cell parameters and composition, $\text{Co}_4\text{Al}_{5.5}\text{Si}_{2.8}$ can be assigned as the δ phase ($\text{Co}_3\text{Al}_4\text{Si}_2 \approx 3/4 \times \text{Co}_4\text{Al}_{5.5}\text{Si}_{2.8}$) of the Co–Al–Si system,¹⁷ it exhibits an incommensurately modulated structure, which will be described in a future publication.

Perhaps more important than its place in the TM–Al–Si phase diagrams is the clue that $\text{Fe}_8\text{Al}_{17.4}\text{Si}_{7.6}$ provides to the roles electron count can play in determining the structures of TM-based intermetallics. Electronic structure calculations point to a surprisingly simple bonding picture for this phase: its complex structure serves to provide the Fe atoms with an 18 electron count. In this way, this phase provides a stepping stone toward understanding the origin of the host–guest structure of $\text{Fe}_{25}\text{Al}_{78}\text{Si}_{20}$ (Figure 1), and forms a bridge between the TM chemistries of molecular complexes and metallic solids.

TECHNICAL PROCEDURES

Synthesis. Fe (Strem chemicals, 99.9%), Al (Alfa Aesar, 99.9%), Si (Strem chemicals, 99.999%) were used as starting materials for the synthesis of $\text{Fe}_8\text{Al}_{17.4}\text{Si}_{7.6}$. The mixed molar ratios of Fe:Al:Si near 1:1.83:0.86 were found to consistently lead to crystals of $\text{Fe}_8\text{Al}_{17.4}\text{Si}_{7.6}$. The starting materials were pressed into pellets, and then welded with an arc melting furnace three times on alternating sides for optimal homogeneity. Each sample was then placed in a fused silica tube under

the Ar atmosphere, which was then evacuated and sealed. The tubes were annealed at 600 °C for 24, 72, or 700 h.

Powder X-ray Diffraction Analysis. The phase purity of the samples was assessed using powder X-ray diffraction. Ground samples were poured into 0.5 mm glass capillaries, and data was measured on a Rigaku Rapid II diffractometer using Mo $K\alpha$ radiation, $\lambda = 0.71073 \text{ \AA}$. For each experiment, the diffraction intensities were measured on an image plate detector with an exposure time of 10 min. The resulting frames were converted to curves of intensity vs diffraction angle 2θ in steps of 0.03 degrees. Patterns were analyzed with the programs JADE and JANA2006.

Wavelength-Dispersive X-ray Spectroscopy. To determine the elemental composition of $\text{Fe}_8\text{Al}_{17.4}\text{Si}_{7.6}$, wavelength dispersive X-ray spectroscopy (WDS) measurements were made. The sample whose powder diffraction pattern showed the highest agreement to that simulated for $\text{Fe}_8\text{Al}_{17.4}\text{Si}_{7.6}$ (annealing time = 72 h) was immersed in non-conductive epoxy at the opening of an aluminum tube. Once the epoxy had hardened, the surface was sanded against diamond paper (up to 0.04 μm) using a polish-wheel with a colloidal silica suspension (Allied High Tech Products, Inc., 0.04 μm), and coated with 250 nm of graphitic carbon. The polished sample was then inspected with a Cameca SX-51 electron microprobe (voltage = 15 kV). Several choices of standards were tested. The sum of the percentages was closest to 100% when an FeAlSi alloy ($\text{Fe}_{19.3}\text{Al}_{69.8}\text{Si}_{10.9}$) was used as a standard for Fe, Al and Si.

Two phases were apparent in the WDS measurements: one appearing dark in the SEM images, the other relatively bright. The former phase had the composition of $\text{Fe}_8\text{Al}_{17.33(6)}\text{Si}_{7.24(9)}$ (average of 8 measurements), which corresponds well to the $\text{Fe}_8(\text{Al}/\text{Si})_{25}$ composition of the $\text{Fe}_8\text{Al}_{17.4}\text{Si}_{7.6}$ phase. The phase appearing brighter was measured to have a composition of $\text{Fe}_4\text{Al}_{3.47(16)}\text{Si}_{3.29(3)}$ (average of 3 measurements), which can perhaps be assigned to the phase $\text{Fe}_4\text{Al}_4\text{Si}_3$ for which no structure has yet been reported. The presence of this relatively Fe- and Si-rich phase is understandable given that the nominal compositions were somewhat Al-poor relative to the stoichiometry of the title phase.

Single Crystal X-ray Diffraction Measurements. Single crystal X-ray diffraction data for $\text{Fe}_8\text{Al}_{17.4}\text{Si}_{7.6}$ was collected on an Oxford diffraction Xcalibur E diffractometer using graphite monochromatized Mo $K\alpha$ radiation ($\lambda = 0.71073 \text{ \AA}$) at ambient temperature. Run list optimization, as well as the data processing to create a list of integrated peak intensities, the peak search, unit cell determination and refinement, the creation of reciprocal lattice reconstructions, multiscan absorption correction, and frame scaling were performed using the CrysAlis Pro v. 171.35.15 software supplied by the manufacturer. The structure was solved with the charge flipping algorithm²¹ using the program SUPERFLIP,²² and refined by full matrix least squares on F^2 using the program JANA2006.²³ Crystal data are given in Table 1.

Structure Determination and Refinement of $\text{Fe}_8\text{Al}_{17.4}\text{Si}_{7.6}$. A crystal picked from the Fe–Al–Si sample annealed for 24 h above exhibited sharp X-ray diffraction peaks of which $\sim 73\%$ could be indexed with the monoclinic cell $a = 8.58 \text{ \AA}$, $b = 15.25 \text{ \AA}$, $c = 14.18 \text{ \AA}$, $\beta = 94.83^\circ$. Crystals taken from the other samples showed close agreement to these parameters, with the range in cell volumes of 0.5%, which we estimate could correspond to a homogeneity range of about 10% in the fraction of the Si/Al sites occupied by Si. Inspection of reciprocal lattice reconstructions of the frame data for the first crystal mentioned above confirmed the unit cell choice, but also revealed other important features. As can be seen in the reconstruction of the $h0l$ layer (Figure 2), a subgroup of these reflections are particularly strong, and corresponds to a I-centered orthorhombic subcell with dimensions $a_{\text{basic}} = 7.60 \text{ \AA}$, $b_{\text{basic}} = 15.24 \text{ \AA}$, $c_{\text{basic}} = 3.98 \text{ \AA}$. The pseudosymmetry associated with this subcell leads to a twin, whose diffraction pattern appears as the mirror image (taken perpendicular to a_{basic} or c_{basic}) of that originally indexed. This is described by the following twin law: $h' = 1/2 h - 1/2 l$, $k' = k$, $l' = -3/2 h - 1/2 l$.

Once this twin-law was recognized, the structure solution became possible. The structure was solved using the original monoclinic unit cell in the space group $P2_1/c$. The initial structure model was obtained through the charge-flipping algorithm, and additional atomic sites were

Table 1. Crystal Data for $\text{Fe}_8\text{Al}_{17.4}\text{Si}_{7.6}$

chemical formula	$\text{Fe}_8\text{Al}_{17.40}\text{Si}_{7.60}^a$
WDS composition	$\text{Fe}_8\text{Al}_{17.33(6)}\text{Si}_{7.24(9)}$
space group	$P2_1/c$
unit cell: a (Å)	8.5743(2)
b	15.2402(3)
c	14.1749(3)
β (deg)	94.841(2)
cell volume	1845.68(7)
Z	4
Pearson symbol	$mP132$
cryst. dimensions (mm^3)	$0.02 \times 0.14 \times 0.18$
crystal color	metallic black
crystal habit	plate
data collection temp.	RT
radiation source, λ (Å)	Mo, $K\alpha$ (0.7107)
absorption coefficient (mm^{-1})	7.425
absorption correction	multiscan
min/max transmission	0.58, 1.00
θ_{min} , θ_{max}	3.58, 28.96
number of reflections	17769
unique refl. [all, $I > 3\sigma(I)$]	4454, 2362
refinement method	F^2
R_{int} [all, $I > 3\sigma(I)$]	3.34, 2.05
number of parameters	299
$R[I > 3\sigma(I)]$, $R_w[I > 3\sigma(I)]$	0.0213, 0.0405
$R(\text{all})$, $R_w(\text{all})$	0.0487, 0.0421
$S[I > 3\sigma(I)]$, $S(\text{all})$	1.67, 1.23
$\Delta\rho_{\text{max}}$, $\Delta\rho_{\text{min}}$ ($e^-/\text{Å}^3$)	1.02, -1.12

^aThe chemical formula was determined as follows: the Fe:(Al/Si) ratio is taken from the single crystal X-ray diffraction results, while the Al:Si ratio (which cannot be meaningfully determined from the diffraction data) is taken from the WDS results.

identified from the difference Fourier map. In this way, a structure model was obtained with 33 independent atomic sites, and the composition $\text{Fe}_8(\text{Al/Si})_{25}$ (with Al atoms being preliminarily placed on the Al/Si sites).

Assignment of Al and Si to the Al/Si sites was based on atomic distances.²⁴ The Si/Al positions were found to fall into two groups: some with Fe-(Si/Al) distances in the range of 2.42 to 2.71 Å, and others with Fe-(Si/Al) distances in the range of 2.27 to 2.49 Å. While these ranges are slightly overlapping, for all of the Si/Al sites in the first group the majority of the Fe-(Si/Al) distances are >2.5 Å, while for the remaining sites all Fe-(Si/Al) distances are <2.5 Å. Assigning Al to the first group and Si to the second group leads to the formula $\text{Fe}_8\text{Al}_{16}\text{Si}_9$. This stoichiometry is close to the WDS composition $\text{Fe}_8\text{Al}_{17.33(6)}\text{Si}_{7.24(9)}$, but is somewhat Al-poor and Si-rich. The discrepancy is likely due to partial occupation of some of the Si sites by Al, a feature that is difficult to detect because of the similar scattering powers of Si and Al. In the final refinement, the Si-rich sites were assigned as 84% Si and 16% Al sites so that the overall Si/Al ratio for the phase matched that of the WDS data. Given (1) the possible homogeneity range of the phase, and (2) the likelihood of the different sites having different ratios of Si and Al, the treatment of the mixed Si/Al sites should be regarded only as a simplistic but convenient approximation.

Electronic Structure Calculations. GGA-DFT calculations were performed on NiSi_2 , CoSi_2 , and $\text{Fe}_8\text{Al}_{17.4}\text{Si}_{7.6}$ (approximated as $\text{Fe}_8\text{Al}_{16}\text{Si}_9$, with the 84:16 Si/Al sites being simplistically treated as being occupied by Si) using the Vienna Ab initio Simulation Package (VASP).²⁵ All calculations were carried out in the high-precision mode, using the PW91 exchange-correlation functional,²⁶ and the projector augmented wave potentials provided with the package.^{25a,d} For NiSi_2 , CoSi_2 , and $\text{Fe}_8\text{Al}_{16}\text{Si}_9$ these settings corresponded to energy cut-offs of respectively 337.0, 335.0, and 334.9 eV. Calculations on the

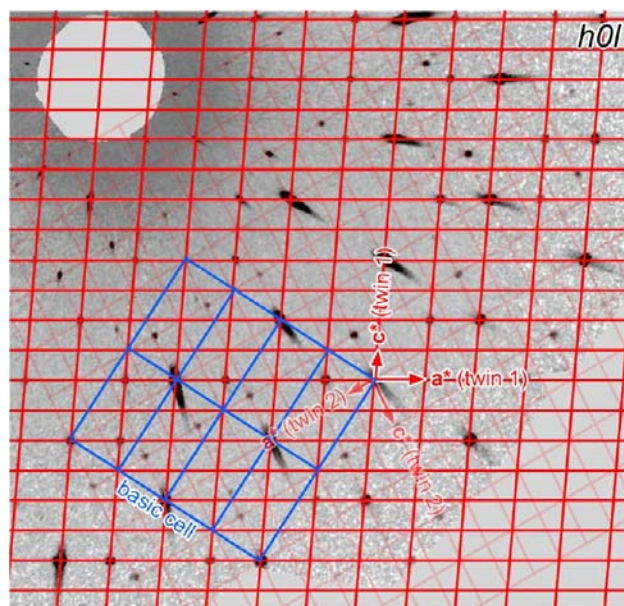


Figure 2. Reciprocal reconstruction of the $h0l$ layer of the single crystal X-ray diffraction data for $\text{Fe}_8\text{Al}_{17.4}\text{Si}_{7.6}$. The pseudosymmetry arising from the presence of an orthorhombic subcell (blue grid) leads to twinning with two orientations of the $\text{Fe}_8\text{Al}_{17.4}\text{Si}_{7.6}$ reciprocal lattice (bold and faded red grids). Further details concerning the crystal and structure refinement are listed in Table 1. The atomic coordinates, atomic displacement parameters, and selected interatomic distances are given in the Supporting Information, Tables S1 and S2.

fluorite-type structures began with a unit cell optimization using a relatively coarse $7 \times 7 \times 7$, Γ -centered k -point grid. Band energies and density of states (DOS) distributions were then calculated using a finer mesh ($11 \times 11 \times 11$, Γ -centered). Because of $\text{Fe}_8\text{Al}_{16}\text{Si}_9$'s large cell size, calculations on it were performed using the experimentally determined coordinates, using a $7 \times 3 \times 3$, Monkhorst–Pack k -point mesh.²⁷

Projected DOS curves were created by drawing spheres around the atomic positions, and projecting the portions of the wave functions within the spheres onto spherical harmonics. As suggested by the VASP manual, the radii were chosen such that the sphere volumes of the atoms within the unit cell summed to the cell volume, and the radius ratios equaled those of the atomic radii. In this case, the radius ratios were drawn from the Wigner-Seitz radii listed in the potential files, leading to the following sphere radii: 1.455 (Ni) and 1.485 Å (Si) in NiSi_2 , 1.446 (Co) and 1.457 Å (Si) in CoSi_2 , and 1.439 (Fe), 1.550 Å (Al) and 1.450 Å (Si) in $\text{Fe}_8\text{Al}_{17.4}\text{Si}_{7.6}$. The electron density isosurfaces of Figure 6 were plotted with the program VESTA 3.²⁸

The VASP band energies and density of states curves were used as the basis for the refinement of simple Hückel models for NiSi_2 and $\text{Fe}_8\text{Al}_{16}\text{Si}_9$ with the program eHtuner,²⁹ with the actual Hückel calculations being carried out by the YAeHMOP program.³⁰ The Hückel parameters used are listed in the Supporting Information, Table S3, along with notes on the parameterization process. For the MO diagrams in Figures 7–9, Hamiltonian matrices for $\text{TM}(\text{Si/Al})_n$ molecular clusters were calculated with YAeHMOP. MATLAB scripts were then written to read in the Hamiltonian matrices, transform them into bases containing the TM atomic orbitals and Si/Al sp^3 hybrid orbitals, and finally determine the eigenvectors and eigenvalues for the $\text{TM}(\text{Si/Al})_n$ systems.

■ THE CRYSTAL STRUCTURE OF $\text{Fe}_8\text{Al}_{17.4}\text{Si}_{7.6}$

As with $\text{Fe}_{25}\text{Al}_{78}\text{Si}_{20}$, the crystal structure of $\text{Fe}_8\text{Al}_{17.4}\text{Si}_{7.6}$ is closely related to the fluorite type structure adopted by CoSi_2 and NiSi_2 . This relationship is most clearly seen by comparing a $[110]$ view of the fluorite structure with a projection down the

[101] direction of the $\text{Fe}_8\text{Al}_{17.4}\text{Si}_{7.6}$ structure (Figure 3). In viewing the fluorite type down the [110] direction (Figure 3a), the cubes of Si appear with their edges up, while the TM atoms (green) lie in the rectangular spaces between raised edges. If we take any one of the Si cubes of this layer, say the one indicated in red, and look beneath it, we find that it is part of a chain of edge sharing cubes running along the [110] direction. Each of the square faces of this chain is capped with TM atoms so that the cubes are ensheathed within TM octahedra (Figure 3a, bottom).

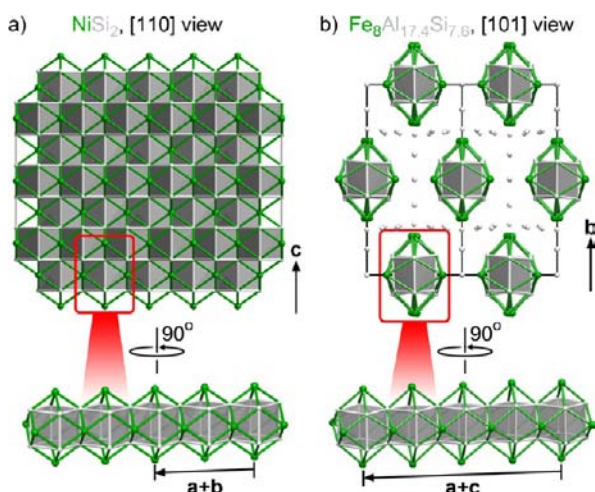


Figure 3. Fragmentation of the fluorite type in the crystal structure of $\text{Fe}_8\text{Al}_{17.4}\text{Si}_{7.6}$. A comparison of views of (a) the fluorite structure, and (b) $\text{Fe}_8\text{Al}_{17.4}\text{Si}_{7.6}$ down respectively the [110] and [101] directions reveals that the Fe–Si–Al phase is built from columns of the fluorite type separated by interfaces one atom thick.

The [101] direction of $\text{Fe}_8\text{Al}_{17.4}\text{Si}_{7.6}$ exhibits similar columns, with Si/Al atoms³¹ forming chains of edge sharing cubes, and Fe atoms capping the square faces of the cubes (Figure 3b). However, while in the fluorite structure the chains occur as part of an infinite cubic network, the columns of $\text{Fe}_8\text{Al}_{17.4}\text{Si}_{7.6}$ occur individually. Each column is surrounded on all four sides by regions not conforming to the fluorite type. The structure of this compound can then be understood in terms of a rod packing of fluorite-type columns, with interface regions one atom thick separating the columns. Two types of interfaces can be discerned: (1) those in which the cube edges meet cube edges along the horizontal direction of Figure 3, and (2) those at which the Al/Si cube faces meet along the vertical direction of Figure 3. We will refer to these as the *edge-to-edge* and *face-to-face* interfaces, respectively.

In Figure 4, we look more closely at these interfaces. To do this, we divide the structure into slabs cut perpendicular to b , with one slab (pink) containing a face-to-face interface, and another (blue) containing a sheet of fluorite-type columns separated by edge-to-edge interfaces. By laying the face-to-face slab out flat (Figure 4b), we see that the Fe atoms from the fluorite columns above (green) and below (yellow) combine to trace out a corrugated hexagonal net. Interfacial Si/Al atoms are nestled into the spaces between these Fe atoms. The majority of these atoms occur in the triangles of the Fe network. Were all the Si/Al atoms to occupy these positions, they would form a simple honeycomb network. Instead, pairs of atoms in this hypothetical honeycomb net have been replaced with single atoms which bridge neighboring Fe atoms. The result is the

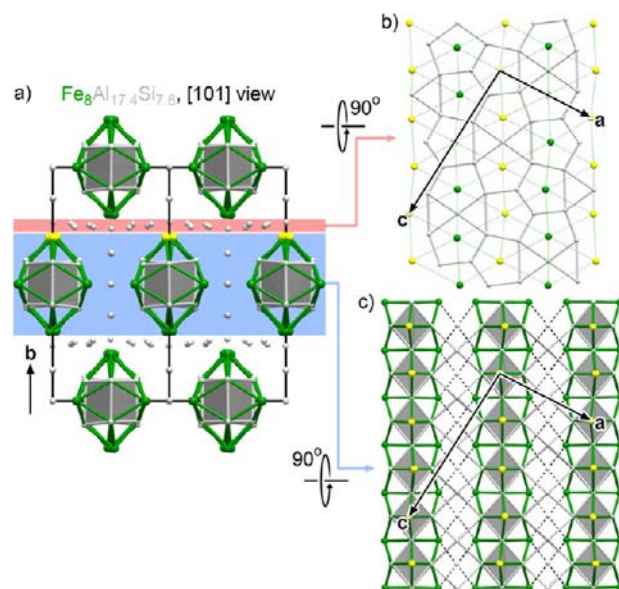


Figure 4. $\text{Fe}_8\text{Al}_{17.4}\text{Si}_{7.6}$ crystal structure. (a) This structure can be understood by dividing it into two types of slabs cut perpendicular to b . (b) The slab highlighted in pink consists of a net of Al/Si atoms (gray) occurring between a corrugated hexagonal array of Fe atoms (green for those coming from above, yellow for those coming from below). (c) The layer highlighted in blue consists of a row of fluorite-type columns, with interface atoms occurring between them. The atoms in yellow in (b) and (c) are shared between the two slabs.

creation of distorted pentagons of Si/Al (rather than ideal hexagons) around the Fe. The coordination environment of each Fe atom is completed by the addition of an Al from across the face of its pentagon (not shown), to yield a total of ten Al/Si neighbors.

A quite different structural motif is seen at the edge-to-edge interfaces (Figure 4c). Here Al atoms occupy the space between the fluorite columns to continue the cubic network of the Si/Al atoms, and fill the resulting interfacial cubes. In the process, the Fe atoms at this interface are coordinated in a bicapped-cubic fashion. These Fe atoms are thus also ten coordinate, an increase of two over the Si_8 cubes available in the fluorite type (a detail that will be important in our discussion of the bonding in this compound).

A nearly identical arrangement of fluorite-type columns is observed in the crystal structure reported for the phase FeAl_2Si .¹² The essential difference between the $\text{Fe}_8\text{Al}_{17.4}\text{Si}_{7.6}$ and FeAl_2Si structures is in the placement of Si/Al atoms in the face-to-face interface layers. Whereas in $\text{Fe}_8\text{Al}_{17.4}\text{Si}_{7.6}$, this layer serves to provide pentagons around all of the Fe atoms above and below, in FeAl_2Si the corresponding layers are more sparsely populated by Si/Al, leaving some of the pentagons with a missing vertex.

In this way, $\text{Fe}_8\text{Al}_{17.4}\text{Si}_{7.6}$ and FeAl_2Si can both be viewed as superstructures of the basic cell indicated in the reciprocal lattice reconstruction of Figure 2. Such similarities could lead to the suspicion that the two structures represent different solutions to the same phase. The reciprocal lattice corresponding to the FeAl_2Si supercell shows little overlap with the superstructure reflections observed for $\text{Fe}_8\text{Al}_{17.4}\text{Si}_{7.6}$, leading us to conclude that these are indeed different compounds.

BONDING IN $\text{Fe}_8\text{Al}_{17.4}\text{Si}_{7.6}$ AND RELATED PHASES

What causes the fragmentation of the fluorite type observed in $\text{Fe}_8\text{Al}_{17.4}\text{Si}_{7.6}$? As a first step in answering this question, we carried out GGA-DFT electronic structure calculations on $\text{Fe}_8\text{Al}_{17.4}\text{Si}_{7.6}$ (approximated as $\text{Fe}_8\text{Al}_{16}\text{Si}_9$ through rounding the occupancies of mixed Al/Si sites) and the fluorite structure, as exemplified by NiSi_2 and CoSi_2 . The resulting electronic density of states (DOS) distributions provide an important clue into the factors stabilizing these compounds (Figure 5). For each of the three phases, the Fermi energy (E_F) lies inside a deep well in the DOS curve that occurs just above a dense block of TM 3d states.

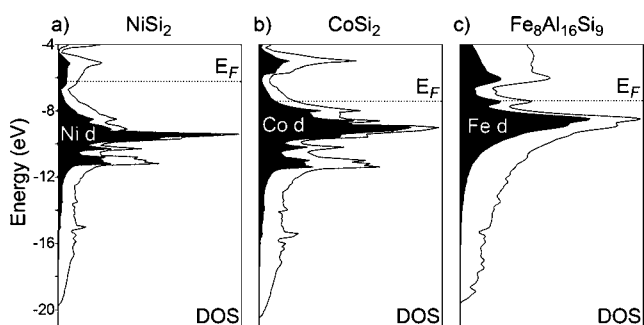


Figure 5. GGA-DFT electronic density of states curves for (a) fluorite-type NiSi_2 , (b) fluorite-type CoSi_2 , and (c) a model of $\text{Fe}_8\text{Al}_{17.4}\text{Si}_{7.6}$ in which the fraction of Si on the mixed Si/Al sites rounded to the nearest integer to give the formula $\text{Fe}_8\text{Al}_{16}\text{Si}_9$. Contributions from the TM d states are shaded in black.

The E_F of NiSi_2 occurs just above a DOS minimum, while that of CoSi_2 lies below such a minimum.³² This observation suggests that for both phases their valence electron count fills the DOS distribution up to a pseudogap, a feature frequently associated with stability in silicides and intermetallic phases in the same way that large HOMO–LUMO gaps provide an indication of low reactivity for molecules.

The shape of the DOS curve near the E_F is more complicated for the model of $\text{Fe}_8\text{Al}_{17.4}\text{Si}_{7.6}$. Here, the E_F sits at a small peak in the DOS.³³ However, this peak occurs in the midst of a deeper hole in the DOS stretching from about -6 to -9 eV, and the partial replacement of the Si sites with Al as is indicated by the WDS data would tend to lower the E_F below this small peak. To a large extent, then, the pseudogaps near the E_F for NiSi_2 and CoSi_2 are preserved in $\text{Fe}_8\text{Al}_{17.4}\text{Si}_{7.6}$.

A central question is thus what interactions underlie the DOS pseudogaps. The nature of the combinations of elements involved makes traditional inorganic electron counting difficult. While TMs are typically placed in the role of cations, to which main group atoms are bound as ligands, the electronegativity differences here do not support such a description. The electronegativities of Ni, Co, Fe, and Si are all essentially equal (~ 1.8), and above that of Al (1.5).³⁴ In this way, it seems appropriate to take a more covalent view of the bonding in these compounds.

An approach to building such a covalent bonding scheme can be found by comparing the valence electron density calculated for NiSi_2 with that of a system that is clearly dominated by covalent interactions: elemental Si.³⁵ This comparison is made in Figure 6, where the structures of Si and NiSi_2 are overlaid with isosurfaces of their electron density distributions.

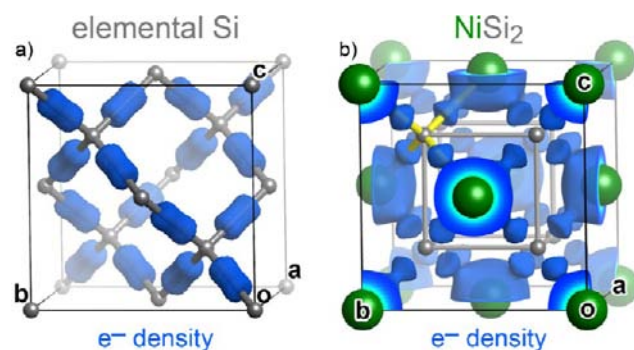


Figure 6. Comparison of the GGA-DFT valence electron density distributions for (a) the sp^3 hybridized atoms of elemental Si, and (b) the NiSi_2 structure. Isosurfaces are drawn for (a) and (b) at the values 0.47 and 0.44 electrons/ \AA^3 , respectively. Si: gray, Ni: green.

The electron density isosurface for elemental Si can be readily interpreted (Figure 6a). Si adopts the diamond structure, in which each atom is tetrahedrally coordinated. The isosurface consists of barrels (somewhat contracted around the middle) situated along the interatomic contacts, representing the concentration of electrons in the regions of the Si–Si bonds. The tetrahedral arrangement of these barrels around each Si atom is consistent with the notion that these atoms are sp^3 hybridized, with one sp^3 hybrid orbital pointed along each bond.

In Figure 6b, we turn to the corresponding surface for NiSi_2 . The isosurface is dominated by a high concentration of electrons surrounding the Ni atoms, as expected considering the high occupation of the relatively contracted Ni 3d orbitals. If we shift our attention to the Si atoms (gray spheres), similarities to the plot for elemental Si become apparent. The Si atoms are again coordinated tetrahedrally (this time by Ni) as is emphasized for one Si with yellow bars. Also as in elemental Si, each of these contacts is marked with a relatively high concentration of electron density.

Such parallels between the electron density distribution surrounding the Si atoms in elemental Si and NiSi_2 suggest a straightforward way of viewing the bonding in NiSi_2 : we can envision the Si atoms as sp^3 hybridized, with one hybrid orbital pointing toward each of its neighbors.³⁶ Each Ni atom would then be surrounded by a cube of sp^3 hybrid orbitals pointing toward it in a σ fashion, as might be represented with the formula $\text{Ni}(\text{Si } \sigma)_8$.

The coordination of a TM atom with a series of σ -orbitals can be easily explored with molecular orbital models. To create such a model, we began by using our GGA-DFT results as a basis for the parameterization of a simple Hückel model for NiSi_2 . Using our program eHtuner,²⁹ the Hückel band structure and DOS curves of NiSi_2 were refined against those calculated with GGA-DFT. The resulting Hückel band energies exhibited reasonable agreements with their DFT counterparts: the root-mean-squared deviation is only 0.12 eV up to 1 eV above the E_F , using a basis set of Ni 4s, 4p, and 3d orbitals and Si 3s and 3p orbitals.

With this effective Hückel model of the DFT results in place, the MO diagram for the $\text{Ni}(\text{Si } \sigma)_8$ system can be constructed. First, a Ni atom is placed inside of a cube of Si as in NiSi_2 . Next, on each Si atom, an sp^3 hybrid orbital is constructed from 3s and 3p functions pointing toward the Ni. Symmetry-adapted linear combinations (SALCs) of these sp^3 hybrids are then taken to obtain functions that transform as irreducible

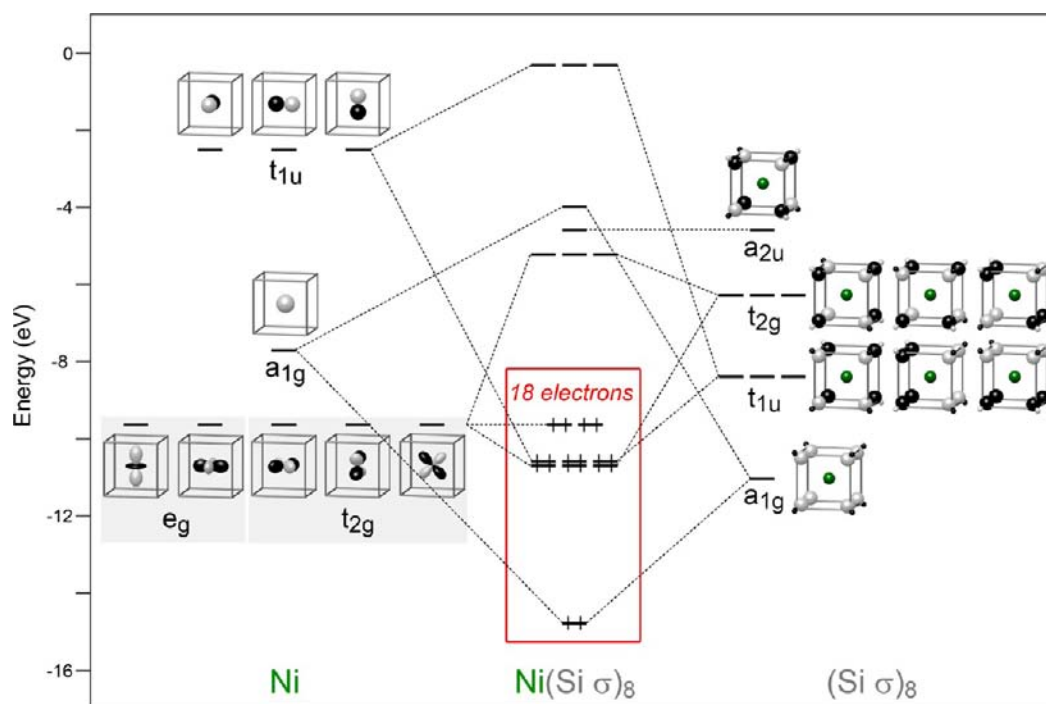


Figure 7. Molecular orbital diagram for a Ni atom coordinated in a cubic geometry by eight Si sp^3 hybrid orbitals.

representations of the O_h point group of the system ($\Gamma_\sigma = a_{1g} + t_{1u} + t_{2g} + a_{2u}$). Once these Si-based SALCs are constructed, we can follow their interactions with the Ni orbitals through a traditional molecular orbital diagram (now made quantitative through our parameterization of the Hückel parameters against DFT), as is shown in Figure 7.

In this diagram, the atomic orbitals of the Ni atom are drawn to the left, with the 3d orbitals ($e_g + t_{2g}$) lying lowest in energy near -10 eV, followed by the 4s (a_{1g}) at ~ -8 eV and the 4p (t_{1u}) at ~ -2.5 eV. The Si σ SALCs are drawn to the right, where they appear spread over a similar energy range as the Ni levels. The dispersion of the Si-based levels derives from Si–Si interactions along the cube edges at a distance of 2.5 Å; the highest is sufficiently antibonding that its energy is not only above the Ni 3d but also the Ni 4s.

The center of the diagram shows the MO energy levels that result from the interactions between the Ni and Si orbitals. The t_{2g} Ni 3d, a_{1g} Ni 4s and t_{1u} Ni 4p orbitals each interact with the Si σ orbitals of the same symmetry, leading to seven bonding and seven antibonding levels. The e_g Ni 3d orbitals find no partners on the Si, and yield two nonbonding orbitals just a little above the highest bonding ones. The a_{2u} Si orbital likewise engages in no Ni–Si interactions, but the Si–Si antibonding within this function is sufficiently high that it ends up among the Ni–Si antibonding levels in energy.

The distribution of energy levels that results bears a striking similarity to those of molecular TM complexes with σ ligands. The interaction of the Ni's nine s, p, and d orbitals gives rise to nine bonding and nonbonding levels. This is followed by a sizable energy gap and then a series of antibonding levels. The result is that the number 18 appears as a propitious electron count. The scheme of Figure 7 is in fact nearly isolobal³⁷ to that of a TM complex coordinated in a cubic fashion by σ donors for which the classic 18 electron rule is expected to apply. The main difference is that the Si σ levels are centered at nearly the same energy as the Ni orbitals, rather than interacting with

below. This leads to some Si–Si antibonding states being left unoccupied, resulting in some net Si–Si bonding. As we begin to consider how this diagram should be populated by electrons for $NiSi_2$, we come to an encouraging result. The valence electron count for this compound is $10 + 4 \times 2 = 18$ per Ni atom, meaning that each Ni atom would have the proper number of electrons to fill all of the bonding and nonbonding levels associated to it.

The large HOMO–LUMO gap for this cluster model recalls the large DOS pseudogap calculated to occur for $NiSi_2$ near the E_F . Other correspondences become apparent when we place the MO energy levels for the $Ni(Si \sigma)_8$ system alongside the DOS curve for the full compound (Figure 8). The $NiSi_2$ DOS pseudogap and E_F both coincide along the energy axis with the HOMO–LUMO gap for $Ni(Si \sigma)_8$ with 18 electrons. Moreover, the peaks in the DOS curve align approximately with the $Ni(Si \sigma)_8$ energy levels. For instance, the sharp DOS peak just above -10 eV matches nearly exactly the MO energy levels for the noninteracting e_g Ni 3d. The broad parabolic region of the DOS below the Ni 3d states appears to be centered at about the same energy as the lowest a_{1g} level of $Ni(Si \sigma)_8$, which was derived from stabilization of the symmetric combination of the Si σ lobes by interaction with the Ni 4s from above.

These results indicate that we may approximate the electronic structure of $NiSi_2$ as being derived from the Ni–Si σ interactions as captured in the MO diagram of Figure 7. Embedding such localized orbitals in the full crystal can simply be viewed as broadening of the distributions of their energy levels through the creation of bands.³⁸

How does this bonding picture transfer to $Fe_8Al_{17.4}Si_{17.6}$? It is helpful to begin our analysis of this more complicated structure by starting with $NiSi_2$ and considering the effect of replacing Ni with Fe and some Si with Al to yield a hypothetical fluorite-type compound with the composition $FeSi_{2-x}Al_x$. Through both substitutions, the valence electron count is lowered, which

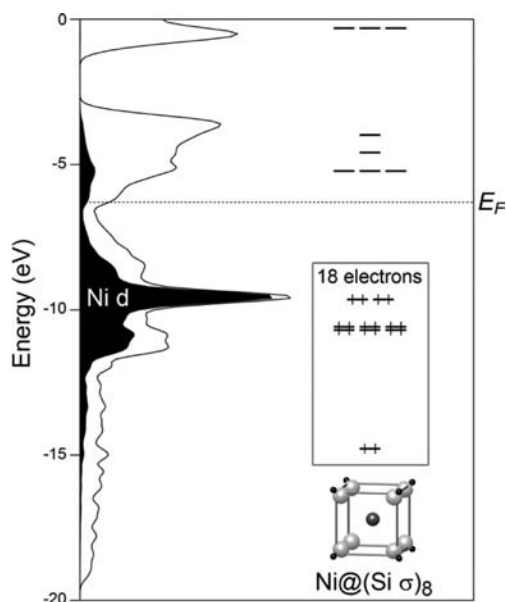


Figure 8. Comparison of the DFT-Calibrated Hückel DOS distribution of NiSi_2 with the MO energy levels for a Ni atom coordinated by eight Si sp^3 hybrid orbitals arranged in a cube.

would be expected to make the TM atoms increasingly electron poor relative to the ideal count of 18 electrons. One solution to this electron deficiency would be to bring in additional Al atoms beyond the $\text{Fe}(\text{Si}/\text{Al})_2$ stoichiometry to increase the total number of electrons per Fe atom. The composition of $\text{Fe}_8\text{Al}_{17.4}\text{Si}_{7.6}$ can be interpreted in just this way. If we regard the Si atoms in this formula as having originated in the hypothetical fluorite-type phase, the compound can be rewritten as $(\text{FeSi}_{0.95}\text{Al}_{1.05})_8(\text{Al})_9$. Adding up the number of valence electrons per Fe for this formula leads us to 18.3.

Empirically, then, $\text{Fe}_8\text{Al}_{17.4}\text{Si}_{7.6}$ appears to be in approximate accordance with the 18 electron rule. The orbital interactions underlying this electron count can be explored through a similar process to that for NiSi_2 . We begin by calibrating a Hückel model against the DFT band energies and DOS curves for a version of the structure in which some mixed Si/Al sites (84% Si, 16% Al) are rounded to 100% Si, leading to the stoichiometry $\text{Fe}_8\text{Al}_{16}\text{Si}_9$. Using eHtuner, a model can be achieved that agrees with the DFT band energies with a root-

mean-squared deviation of 0.062 eV (up to 1 eV above the E_F).³⁹ We then go through the 8 symmetry-inequivalent Fe sites, and create MO diagrams assuming that each Al/Si neighbor has an sp^3 hybrid orbital directed at the Fe.

The resulting MO levels for the Fe sites are displayed alongside the DFT-calibrated Hückel DOS curve for $\text{Fe}_8\text{Al}_{16}\text{Si}_9$ in Figure 9. As in the MO diagram for $\text{Ni}(\text{Si} \sigma)_8$, a large HOMO–LUMO gap appears at the 18 electron count for each of these $\text{Fe}(\text{Si}/\text{Al} \sigma)_{10}$ polyhedra. Again, there are qualitative correspondences between the energy levels in the MO diagrams, and the features of the DOS curve for the full crystal structure. The most important concerns the DOS depression occurring near the E_F . The HOMO–LUMO gaps for the various Fe sites all span roughly the same energy range, and this range coincides well with the DOS pseudogap in the $\text{Fe}_8\text{Al}_{16}\text{Si}_9$ model of $\text{Fe}_8\text{Al}_{17.4}\text{Si}_{7.6}$.

It appears then that $\text{Fe}_8\text{Al}_{17.4}\text{Si}_{7.6}$ can be regarded as an intermetallic version of an 18 electron complex, in which the stable electron count stems from the optimal use of each TM atom's nine valence orbitals. It now becomes clear what is achieved by the fragmentation of the fluorite structure type to form the structure of $\text{Fe}_8\text{Al}_{17.4}\text{Si}_{7.6}$. The fragmentation serves a structural mechanism by which more Si/Al atoms can be introduced into the coordination environment of the Fe atoms than can be accommodated by the fluorite structure itself. The driving force for doing so is better adherence to the 18 electron rule.

CONCLUSIONS

As in other classes of compounds, electron count plays a key role in the structures of intermetallic phases. In this paper, we have seen how the structure of $\text{Fe}_8\text{Al}_{17.4}\text{Si}_{7.6}$ illustrates one means by which this occurs. Its parent structure, the common fluorite type, derives stability from an orbital interaction scheme with parallels to that of 18 electron TM complexes. Since the Fe and Si/Al atoms involved do not have sufficient numbers of electrons to reach an 18 electron configuration within this structure type, fragmentation of the fluorite structure into columns occurs. The interfaces between columns offer the opportunity to increase the electron density on the Fe through the incorporation of new Si/Al atoms into their coordination environments. In this way, $\text{Fe}_8\text{Al}_{17.4}\text{Si}_{7.6}$ serves as an intermetallic analogue of coordination compounds in the

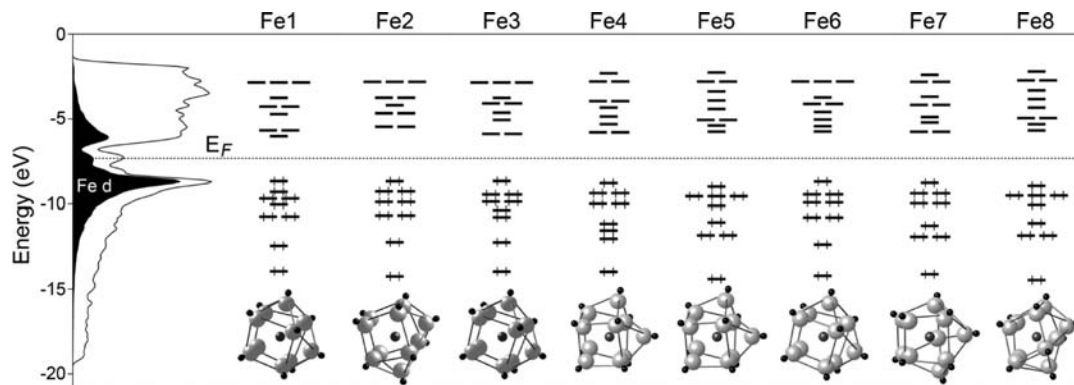


Figure 9. DFT-calibrated DOS curve of $\text{Fe}_8\text{Al}_{17.4}\text{Si}_{7.6}$ (approximated as $\text{Fe}_8\text{Al}_{16}\text{Si}_9$ through the rounding of the occupancies of mixed Si/Al sites) plotted alongside MO energy levels for $\text{Fe}(\text{Al}/\text{Si} \sigma)_{10}$ complexes corresponding to the eight symmetry-inequivalent Fe sites of this structure. The Fermi Energy (E_F) and pseudogap of the full compound coincide with the HOMO–LUMO gaps at 18 electrons for the $\text{Fe}(\text{Al}/\text{Si} \sigma)_{10}$ model clusters. For clarity, MO energy levels for each cluster differing by <0.3 eV are drawn as degenerate.

same way that Zintl phases recall molecules obeying the octet and Wade–Mingos rules.²

This bonding picture for $\text{Fe}_8\text{Al}_{17.4}\text{Si}_{7.6}$ raises the question of how other complex 18-electron compounds might result from perturbations to the fluorite type. Our perusal of other crystal structures reported in the TM–Al–Si systems indicates that fluorite variants are widespread. We already saw in Figure 1 that the structure of $\text{Fe}_{25}\text{Al}_{78}\text{Si}_{20}$ consists of a fluorite-like host lattice in which fragments of the *fcc* structure have been included. Another example is the Ir_3Ge_7 -type phase $\text{Co}_3\text{Al}_3\text{Si}_4$,¹⁶ whose structure can be viewed as a body-centered packing of O_h $\text{Co}_6(\text{Si}/\text{Al})_8$ fluorite clusters. It will be interesting to see through further theoretical work in what ways the desire for filled octadecets influences these phases, as well as what other factors determine their fragmentation patterns.

The 18 electron rule is such a prevalent theme in TM chemistry that it is likely that it applies, perhaps in a variety of guises, to other intermetallics beyond those discussed in this Article. We are hopeful that soon the same electron bookkeeping that has sustained chemists through a vast series of TM complexes may provide similar guidance to intermetallic phases in their continuously unfolding structural diversity.

■ ASSOCIATED CONTENT

■ Supporting Information

Tables of crystallographic data and the Hückel parameters used in the theoretical analysis, as well as the optimized structures of NiSi_2 and CoSi_2 . A Crystallographic Information File (CIF) for $\text{Fe}_8\text{Al}_{17.4}\text{Si}_{7.6}$. This material is available free of charge via the Internet at <http://pubs.acs.org>.

■ AUTHOR INFORMATION

Corresponding Author

*E-mail: danny@chem.wisc.edu.

Notes

The authors declare no competing financial interest.

■ ACKNOWLEDGMENTS

We thank Drs. John Fournelle and Hiromi Konishi at the UW–Madison Dept. of Geosciences for assistance with the EDS/WDS analysis and powder X-ray diffraction measurements, respectively. We also gratefully acknowledge the financial support of the National Science Foundation (NSF) through Grant DMR-1207409, and the Wisconsin Alumni Research Foundation. This research involved calculations using computer resources supported by NSF Grant CHE-0840494.

■ REFERENCES

- (1) Hume-Rothery, W.; Raynor, G. V. *The structure of metals and alloys*, 4th ed.; Institute of Metals: London, U.K., 1962.
- (2) Kauzlarich, S. M. *Chemistry, structure, and bonding of Zintl phases and ions*; VCH: New York, 1996.
- (3) Mitchell, P. R.; Parish, R. V. *J. Chem. Educ.* **1969**, *46*, 811.
- (4) (a) Tobola, J.; Pierre, J.; Kaprzyk, S.; Skolozdra, R. V.; Kouacou, M. A. *J. Magn. Magn. Mater.* **1996**, *159*, 192. (b) Tobola, J.; Pierre, J.; Kaprzyk, S.; Skolozdra, R. V.; Kouacou, M. A. *J. Phys.: Condens. Matter* **1998**, *10*, 1013. (c) Jung, D.; Koo, H. J.; Whangbo, M. H. *J. Mol. Struct. (Theochem)* **2000**, *527*, 113. (d) Tobola, J.; Pierre, J. *J. Alloys Compd.* **2000**, *296*, 243. (e) Kandpal, H. C.; Felser, C.; Seshadri, R. *J. Phys. D: Appl. Phys.* **2006**, *39*, 776. (f) Kohler, J.; Deng, S. Q.; Lee, C.; Whangbo, M. H. *Inorg. Chem.* **2007**, *46*, 1957.
- (5) (a) Roger, J.; Jeanneau, E.; Viala, J. C. *Z. Kristallogr.* **2011**, *226*, 805. (b) Sugiyama, K.; Kaji, N.; Hiraga, K. *J. Alloys Compd.* **2004**, *368*, 251.

- (6) (a) Bertaut, F.; Blum, P. *Compt. rend.* **1950**, *231*, 626. (b) Schubert, K.; Pfisterer, H. *Z. Metallkd.* **1950**, *41*, 433. (c) Wittmann, A.; Burger, K. O.; Nowotny, H. *Monatsh. Chem.* **1961**, *92*, 961.
- (7) Wittmann, A.; Burger, K. O.; Nowotny, H. *Monatsh. Chem.* **1962**, *93*, 674.
- (8) (a) Häussermann, U.; Viklund, P.; Svensson, C.; Eriksson, S.; Berastegui, P.; Lidin, S. *Angew. Chem., Int. Ed.* **1999**, *38*, 488. (b) Viklund, P.; Svensson, C.; Hull, S.; Simak, S. I.; Berastegui, P.; Häussermann, U. *Chem.—Eur. J.* **2001**, *7*, 5143.
- (9) (a) Corby, R. N.; Black, P. J. *Acta Crystallogr.* **1977**, *B33*, 3468. (b) Roger, J.; Bosselet, F.; Viala, J. C. *J. Solid State Chem.* **2011**, *184*, 1120.
- (10) (a) Romming, C.; Hansen, V.; Gjonnes, J. *Acta Crystallogr.* **1994**, *B50*, 307. (b) Hansen, V.; Hauback, B.; Sundberg, M.; Romming, C.; Gjonnes, J. *Acta Crystallogr.* **1998**, *B54*, 351.
- (11) Gueneau, C.; Servant, C.; d'Yvoire, F.; Rodier, N. *Acta Crystallogr.* **1995**, *C51*, 177.
- (12) German, N. V.; Zavodnik, V. E.; Yanson, T. I.; Zarechnyuk, O. S. *Kristallografiya* **1989**, *34*, 738.
- (13) German, N. V.; Bel'skii, V. K.; Yanson, T. I.; Zarechnyuk, O. S. *Kristallografiya* **1989**, *34*, 735.
- (14) Gueneau, C.; Servant, C.; d'Yvoire, F.; Rodier, N. *Acta Crystallogr.* **1995**, *C51*, 2461.
- (15) (a) Yanson, T. I.; Manyako, M. B.; Bodak, O. I.; German, N. V.; Zarechnyuk, O. S.; Cerny, R.; Pacheco, J. V.; Yvon, K. *Acta Crystallogr.* **1996**, *C52*, 2964. (b) Marker, M. C. J.; Skolyszewska-Kühberger, B.; Effenberger, H. S.; Schmetterer, C.; Richter, K. W. *Intermetallics* **2011**, *19*, 1919.
- (16) Burger, K. O.; Wittmann, A.; Nowotny, H. *Monatsh. Chem.* **1962**, *93*, 9.
- (17) Richter, K. W.; Prots, Y.; Grin, Y. *Inorg. Chem.* **2005**, *44*, 4576.
- (18) (a) Richter, K. W.; Prots, Y. *Z. Kristallogr.-New Cryst. Struct.* **2006**, *221*, 115. (b) Wu, X.; Lattner, S.; Kanatzidis, M. G. *Inorg. Chem.* **2006**, *45*, 5358.
- (19) Richter, K. W.; Prots, Y. *Z. Kristallogr.-New Cryst. Struct.* **2006**, *221*, 112.
- (20) (a) Ghosh, G. In *Ternary alloys: a comprehensive compendium of evaluated constitutional data and phase diagrams*; Petzow, G., Effenberger, G., Eds.; VCH: Weinheim, Germany, 1992; Vol. 5, p 394; (b) Schmid Fetzer, R. In *Ternary alloys: a comprehensive compendium of evaluated constitutional data and phase diagrams*; Petzow, G., Effenberger, G., Eds.; VCH: Weinheim, Germany, 1991; Vol. 4, p 254.
- (21) (a) Oszlányi, G.; Sütő, A. *Acta Crystallogr.* **2004**, *A60*, 134. (b) Oszlányi, G.; Sütő, A. *Acta Crystallogr.* **2005**, *A61*, 147.
- (22) Palatinus, L.; Chapuis, G. *J. Appl. Crystallogr.* **2007**, *40*, 786.
- (23) Petříček, V.; Dušek, M.; Palatinus, L. *Jana2006. The crystallographic computing system*; Institute of Physics: Praha, Czech Republic, 2006.
- (24) A nice discussion of using interatomic distances for distinguishing Al and Si is given in ref 9b.
- (25) (a) Blöchl, P. E. *Phys. Rev. B* **1994**, *50*, 17953. (b) Kresse, G.; Furthmüller, J. *Phys. Rev. B* **1996**, *54*, 11169. (c) Kresse, G.; Furthmüller, J. *Comput. Mater. Sci.* **1996**, *6*, 15. (d) Kresse, G.; Joubert, D. *Phys. Rev. B* **1999**, *59*, 1758.
- (26) Perdew, J. P.; Chevary, J. A.; Vosko, S. H.; Jackson, K. A.; Pederson, M. R.; Singh, D. J.; Fiolhais, C. *Phys. Rev. B* **1992**, *46*, 6671.
- (27) Monkhorst, H. J.; Pack, J. D. *Phys. Rev. B* **1976**, *13*, 5188.
- (28) Momma, K.; Izumi, F. *J. Appl. Crystallogr.* **2011**, *44*, 1272.
- (29) Stacey, T. E.; Fredrickson, D. C. *Dalton Trans.* **2012**, *41*, 7801.
- (30) Landrum, G. A. *YAEHMOP: Yet Another extended Hückel Molecular Orbital Package*, Version 3.0; YAEHMOP is freely available on the WWW at URL: <http://sourceforge.net/projects/yaehmop/>
- (31) Because of the difficulty of definitively distinguishing Si from Al using single crystal X-ray diffraction data, in our structural description we will refer to most positions as either TM or Si/Al sites.
- (32) (a) Tersoff, J.; Hamann, D. R. *Phys. Rev. B* **1983**, *28*, 1168. (b) Kudrnovský, J.; Christensen, N. E. *Solid State Commun.* **1991**, *78*, 153.

(33) The presence of Fe d character at the E_p , albeit small, introduces the possibility of magnetic ordering in this phase. Magnetic property measurements on this phase are complicated by our inability to obtain phase pure samples. We have carried out preliminary magnetization measurements on our samples with nominal composition $\text{Fe}_1\text{Al}_{1.82}\text{Si}_{0.86}$. For fields above ~ 0.5 T, the magnetization curve becomes dominated by a diamagnetic effect. Upon making a linear correction to the magnetization data, a small ferromagnetic effect is observed, with a saturation moment at 6 K of 0.14 emu/g. As this corresponds to only $0.0032 \mu_B/\text{Fe}$ atom, this effect should probably be attributed to a ferromagnetic impurity rather than to phase of interest. These results support the non-spin-polarized treatment of the electronic structure of $\text{Fe}_8\text{Al}_{17.4}\text{Si}_{7.6}$ given in this paper.

(34) Fredrickson, D. C.; Lee, S.; Hoffmann, R.; Lin, J. *Inorg. Chem.* **2004**, *43*, 6151.

(35) The electron density (as well as the electron localization function) of elemental Si was used similarly as a standard for sp^3 hybridization in ref 4e.

(36) In ref 32a., similar conclusions were reached regarding the covalent character of the bonding and sp^3 hybridization of the Si in NiSi_2 and CoSi_2 .

(37) Hoffmann, R. *Angew. Chem., Int. Ed.* **1982**, *21*, 711.

(38) (a) Burdett, J. K. *Chemical bonding in solids*; Oxford University Press: New York, 1995; (b) Hoffmann, R. *Solids and surfaces: a chemist's view of bonding in extended structures*; VCH Publishers: New York, 1988.

(39) Better numerical agreement could be obtained through further eHtuner iterations, but the resulting parameters are less chemically intuitive. See note in the Supporting Information, Table S5.